ACADEMIC PRESS

Available online at www.sciencedirect.com

SCIENCE DIRECT®

Journal of Computational Physics 185 (2003) 100–119

JOURNAL OF COMPUTATIONAL PHYSICS

www.elsevier.com/locate/jcp

Development of low-diffusion flux-splitting methods for dense gas–solid flows

Deming Mao [a], Jack R. Edwards [a,*], Andrey V. Kuznetsov [a], Ravi K. Srivastava [b]

[a] *Department of Mechanical and Aerospace Engineering, North Carolina State University, Campus Box 7910, Raleigh, NC 27695, USA*
[b] *U.S. Environmental Protection Agency, Air Pollution Prevention and Control Division, National Risk Management Research Laboratory, Office of Research and Development, Research Triangle Park, NC 27711, USA*

Received 6 February 2002; received in revised form 13 August 2002; accepted 20 August 2002

Abstract

The development of a class of low-diffusion upwinding methods for computing dense gas–solid flows is presented in this work. An artificial compressibility/low-Mach preconditioning strategy is developed for a hyperbolic two-phase flow equation system consisting of separate solids and gas momentum and continuity equations. The eigenvalues of this system are used to devise extensions of the AUSM+ [1] and LDFSS [2] flux-splitting methods that provide high resolution capturing of bubble growth and collapse in gas–solid fluidized beds. Applications to several problems in fluidization are presented.

Keywords: Upwind discretization; Time-derivative preconditioning; Two-phase flow; Fluidization

1. Introduction

Fluidized bed reactors are prevalent in many industrial settings, and an accurate prediction of their response under different operating conditions has been a goal in multi-phase computational fluid dynamics for many years [3–10]. Pioneering works, such as that of Gidaspow and co-workers ([3], and references cited within), utilized classical pressure-based methods combined with somewhat diffusive upwind or hybrid schemes to compute many problems of technical interest. Sophisticated closures for solids viscosity and solids pressure (which acts to prevent solids compaction to zero voidage) were later introduced [4,5], with a view toward improving predictions with experimental data. Such data are invariably three-dimensional, with wall effects and multi-port injection of gas and solids all contributing to the gas–solid mixing patterns, but many pioneering contributions idealized the process by assuming either two-dimensionality or axi-

* Corresponding author. Tel.: 1-919-515-5264; fax: 1-919-515-7968.
E-mail addresses: dmao@eos.ncsu.edu (D. Mao), jredward@eos.ncsu.edu (J.R. Edwards), avkuznet@eos.ncsu.edu (A.V. Kuznetsov), srivastava.ravi@epa.gov (R.K. Srivastava).

0021-9991/02/$ - see front matter
PII: S0021-9991(02)00049-9

symmetry. Approaching the literature from a different perspective, one is left wondering whether such sophisticated closures are actually necessary if one utilizes high-resolution numerical schemes on well-resolved, three-dimensional domains with proper treatment of geometrical effects.

The present work is designed to progress toward this "large-eddy simulation" level of modeling of fluidized-bed reactor physics. The first step, presented in this paper, involves the development of high-resolution methods for the computation of dense gas–solid flows. The approach differs from those in [6–10] in that the techniques are developed within an overall framework of time-derivative preconditioning, which enables strong coupling of the governing equations and a reconciliation of widely differing characteristic speeds within the system. Attention is focused on the hyperbolic two-fluid model of Gidaspow [3], specialized for incompressible gas–solid flows and augmented by the addition of a solids pressure model proposed by Boivin et al. [10] With this basis, preconditioning techniques for solving the equation system for incompressible solids- and gas-phases are developed. The resulting eigenvalues are used to define extensions of the AUSM+ [1] and LDFSS [2] low-diffusion upwind schemes suitable for high-resolution simulations of fluidized-bed phenomena. Applications to several problems in fluidization conclude the paper.

2. Governing equations

The developments outlined herein are based on Gidaspow's hydrodynamics model B [3], a gas–solids model that is rendered hyperbolic by concentrating gas pressure effects solely within the gas-phase and solids pressure effects within the solids-phase. Here, we modify Gidaspow's model by assuming an incompressible gas-phase; the time matrix for this system is not invertible, and as such, the pressure cannot be updated directly. The preconditioning strategy discussed later circumvents this difficulty. The governing equations are written as

$$\frac{\partial U}{\partial t}+\frac{\partial F}{\partial x}+\frac{\partial G}{\partial y}=S, \tag{1}$$

where

$$U=\begin{bmatrix}\alpha_g\\ \alpha_g u_g\\ \alpha_g v_g\\ \alpha_s\\ \alpha_s u_s\\ \alpha_s v_s\end{bmatrix},\quad F=\begin{bmatrix}\alpha_g u_g\\ \alpha_g u_g^2+p_g/\rho_g\\ \alpha_g u_g v_g\\ \alpha_s u_s\\ \alpha_s u_s^2+p_s/\rho_s\\ \alpha_s u_s v_s\end{bmatrix},$$

$$G=\begin{bmatrix}\alpha_g v_g\\ \alpha_g v_g u_g\\ \alpha_g v_g^2+p_g/\rho_g\\ \alpha_s v_s\\ \alpha_s v_s u_s\\ \alpha_s v_s^2+p_s/\rho_s\end{bmatrix},\quad S=\begin{bmatrix}0\\ C(u_g-u_s)/\rho_g\\ g+C(v_g-v_s)/\rho_g\\ 0\\ -C(u_g-u_s)/\rho_s\\ (1-\rho_g/\rho_s)\alpha_s g-C(v_g-v_s)/\rho_s\end{bmatrix}, \tag{2}$$

In this, α_g is the gas-phase void fraction, $\alpha_s=1-\alpha_g$ is the solids-phase void fraction, u_s, u_g, v_s, v_g are the solids- and gas-phase velocities, and g is acceleration due to gravity. The gas-phase intrinsic density ρ_g and the solids-phase intrinsic density ρ_s are assumed constant. The function C scales the momentum exchange terms and is defined as follows:

$$C = 150\left(\frac{\alpha_s}{\alpha_g}\right)^2 \frac{\mu}{d_p^2} + 1.75\rho_g\left(\frac{\alpha_s}{\alpha_g}\right)\frac{|\vec{V}_g - \vec{V}_s|}{d_p}, \quad \alpha_g < 0.8 \tag{3}$$

and

$$C = 0.75 C_D \frac{\alpha_s \rho_g |\vec{V}_g - \vec{V}_s| \alpha_g^{-2.65}}{d_p}, \quad \alpha_g > 0.8. \tag{4}$$

In the preceding expressions, μ is the gas viscosity (assumed constant), d_p is the particle diameter, and C_D is the drag coefficient. The form for the solids pressure is taken from Boivin et al. [10]:

$$p_s = \rho_s C_s \left[\alpha_s + 2\alpha_{s,max} \ln\left(1 - \frac{\alpha_s}{\alpha_{s,max}}\right) - \frac{\alpha_s \alpha_{s,max}}{\alpha_s - \alpha_{s,max}}\right], \tag{5}$$

where $\alpha_{s,max}$ is the solids void fraction at maximum compaction (taken as 0.64) and C_s is a scaling constant (taken as 0.02 for most calculations). A solids "sound speed" can be defined through the relation

$$\rho_s a_s^2 = \frac{\partial p_s}{\partial \alpha_s} = \rho_s C_s \left(\frac{\alpha_s}{\alpha_s - \alpha_{s,max}}\right)^2. \tag{6}$$

The solids sound speed ranges from zero at zero solids voidage to infinity at maximum compaction and varies as the square of the solids voidage in the dilute limit of $\alpha_s \to 0$. It is noted that this two-fluid model has a conservative form, meaning that shock solutions may be easily and uniquely defined. Furthermore, the form chosen for the solids pressure ensures that the maximum principle for the void fraction [9,10] is satisfied.

3. Time-derivative preconditioning

To enable time evolution of this system, artificial time derivatives of gas and solids pressure are added to the continuity and momentum equations. The modified equation system can be expressed as

$$P\frac{\partial V}{\partial t} + \frac{\partial F}{\partial x} + \frac{\partial G}{\partial y} = S, \tag{7}$$

where the vector $V = [p_g, u_g, v_g, \alpha_s, u_s, v_s]$ and the preconditioning matrix P is

$$P = \begin{bmatrix} \frac{1}{\tilde{\rho}\beta_g^2} & 0 & 0 & -1 & 0 & 0 \\ \frac{u_g}{\tilde{\rho}\beta_g^2} & \alpha_g & 0 & -u_g & 0 & 0 \\ \frac{v_g}{\tilde{\rho}\beta_g^2} & 0 & \alpha_g & -v_g & 0 & 0 \\ 0 & 0 & 0 & 1 + \frac{\rho_s a_s^2}{\bar{\rho}}\theta_s & 0 & 0 \\ 0 & 0 & 0 & u_s\left(1 + \frac{\rho_s a_s^2}{\bar{\rho}}\theta_s\right) & \alpha_s & 0 \\ 0 & 0 & 0 & v_s\left(1 + \frac{\rho_s a_s^2}{\bar{\rho}}\theta_s\right) & 0 & \alpha_s \end{bmatrix}. \tag{8}$$

In this, β_g is a reference velocity for the gas-phase, θ_s is a scaling parameter, defined as $\theta_s = (1/\beta_s^2) - (1/a_s^2)$, and β_s is a reference velocity for the solids-phase. The quantities $\tilde{\rho}$ and $\bar{\rho}$ are reference densities. Precise forms for all of these will be defined later. The eigenvalues of $P^{-1}A$, where $A = (\partial F/\partial V)$ are

$$u_g, \quad \frac{1}{2}\left(u_g \pm \sqrt{u_g^2 + 4\frac{\tilde{\rho}}{\rho_g}\beta_g^2}\right), \quad u_s, \quad \frac{1}{2}\left[(1 + M_{ref}^2)u_s \pm \sqrt{u_s^2(1 - M_{ref}^2)^2 + 4a_s^2 M_{ref}^2}\right], \tag{9}$$

where

$$\frac{1}{M_{\mathrm{ref}}^2} = 1 + \frac{\rho_{\mathrm{s}}}{\bar{\rho}} \frac{1 - M_{\mathrm{s}}^2}{M_{\mathrm{s}}^2}, \tag{10}$$

$$M_{\mathrm{s}}^2 = \frac{\beta_{\mathrm{s}}^2}{a_{\mathrm{s}}^2}. \tag{11}$$

It is of note that the eigenvalues corresponding to the gas-phase are identical with those obtained for Chorin's artificial compressibility method, with an effective reference velocity of $((\tilde{\rho}/\rho_{\mathrm{g}})\beta_{\mathrm{g}}^2)^{1/2}$. The eigenvalues corresponding to the solids-phase are identical to those typically resulting from preconditioning matrices of the forms proposed by Turkel [11], Choi and Merkle [12], and Weiss and Smith [13], among others, with a specially defined reference Mach number given by (10).

The choice of the reference velocities β_{g} and β_{s} and the reference densities $\tilde{\rho}$ and $\bar{\rho}$ can have profound effects on the accuracy and efficiency of schemes designed to solve the gas–solid system described above. The following choices for β_{g} and β_{s} are used in this work:

$$\beta_{\mathrm{g}}^2 = \max(u_{\mathrm{g}}^2 + v_{\mathrm{g}}^2, U_{\mathrm{ref,g}}^2), \tag{12}$$

$$\beta_{\mathrm{s}}^2 = \min(a_{\mathrm{s}}^2, \max(u_{\mathrm{s}}^2 + v_{\mathrm{s}}^2, U_{\mathrm{ref,s}}^2)), \tag{13}$$

with $U_{\mathrm{ref,g}}$ and $U_{\mathrm{ref,s}}$ both set to user-specified constants. The forms for β_{g} and β_{s} are consistent with the assumption of an incompressible gas-phase and a "compressible" solids-phase, in the sense that the solids-phase can become more dense or dilute as conditions change. The preconditioning strategy for the solids-phase replaces the solids sound speed by a quantity proportional to β_{s} as the degree of compaction increases. In contrast, a "supersonic flow" situation may prevail for dilute gas–solid flows, as the solids-phase velocity may be much higher than the solids sound speed.

The choice of reference densities $\tilde{\rho}$ and $\bar{\rho}$ is less obvious. The selections $\tilde{\rho} = \rho_{\mathrm{g}}$ and $\bar{\rho} = \rho_{\mathrm{s}}$ render the eigenvalues independent of the density but result in excessively diffuse solutions that do not fluidize at the right conditions for the schemes discussed later. Better choices include $\tilde{\rho} = \bar{\rho} = \rho_{\mathrm{g}}\alpha_{\mathrm{g}} + \rho_{\mathrm{s}}\alpha_{\mathrm{s}} \equiv \rho_{\mathrm{b}}$, the bulk density, and $\tilde{\rho} = \rho_{\mathrm{b}}$, $\bar{\rho} = \rho_{\mathrm{s}}$. The latter choice renders the solids-phase eigenvalues independent of density, while the former means that the bulk continuity equation evolves according to

$$\frac{1}{\rho_{\mathrm{b}}}\left(\frac{1}{\beta_{\mathrm{g}}^2}\frac{\partial p_{\mathrm{g}}}{\partial t} + \theta_{\mathrm{s}}\frac{\partial p_{\mathrm{s}}}{\partial t}\right) + \frac{\partial}{\partial x}(\alpha_{\mathrm{g}}u_{\mathrm{g}} + \alpha_{\mathrm{s}}u_{\mathrm{s}}) + \frac{\partial}{\partial y}(\alpha_{\mathrm{g}}v_{\mathrm{g}} + \alpha_{\mathrm{s}}v_{\mathrm{s}}) = 0. \tag{14}$$

Both choices imply that numerical formulations discussed next will be phase-coupled through the eigenvalues.

4. Flux-splitting schemes

For many two-phase and multi-phase equation systems, determining the characteristic speeds alone is a difficult task, even if the system is constructed so that real eigenvalues result. Determining the associated eigenvectors is an even more time-consuming task. This complexity increases if time-derivative preconditioning techniques need to be introduced to avoid excessive numerical stiffness. It may be of use, therefore, to consider schemes that do not depend on the details of the eigenstructure to a large extent. Examples of such schemes are the Lax–Friedrichs method, which is rather dissipative, and such low-diffusion methods as AUSM+ [1] and LDFSS [2].

Earlier works [1,2] have detailed the development of AUSM+ and LDFSS, both of which combine the the robustness and simplicity of flux-vector splitting methods with the accuracy of flux-difference splitting methods. General procedures for extending these methods to low-Mach gas-phase flows have been presented in [14] and extensions suitable for real fluids undergoing equilibrium phase transitions have been presented in [15]. AUSM-type methods for computing separated two-phase flows are known to be under development by several groups [16–18]. These techniques tend to differ quite widely in their construction. The work of [18] is the closest to the present study but differs in the choice of preconditioning strategy and the use of the low-Mach extensions of [14], which may not be as suited for general fluids.

The present work presents extensions of AUSM+ and LDFSS for the gas–solid system discussed above. The formulation follows from the low-Mach and real-fluid extensions of [14,15].

The interface flux vector F in (7) is split into phasic contributions $F_g + F_s$ as follows:

$$F = \begin{bmatrix} \alpha_g u_g \\ \alpha_g u_g^2 + p_g/\rho_g \\ \alpha_g u_g v_g \\ 0 \\ 0 \\ 0 \end{bmatrix} + \begin{bmatrix} 0 \\ 0 \\ 0 \\ \alpha_s u_s \\ \alpha_s u_s^2 + p_s/\rho_s \\ \alpha_s u_s v_s \end{bmatrix}. \tag{15}$$

Each phasic contribution F_k ($k =$ gas or solids), evaluated at a cell interface, is then further split into convective and pressure contributions $F_{k,1/2} = F^c_{k,1/2} + F^p_{k,1/2}$, which are discretized separately in the following manner:

$$F^c_{k,1/2} = U_k^+ \begin{bmatrix} \alpha_k \\ \alpha_k u_k \\ \alpha_k v_k \end{bmatrix}_L + U_k^- \begin{bmatrix} \alpha_k \\ \alpha_k u_k \\ \alpha_k v_k \end{bmatrix}_R \tag{16}$$

and

$$F^p_{k,1/2} = \begin{bmatrix} 0 \\ p_{k,1/2}/\rho_k \\ 0 \end{bmatrix}. \tag{17}$$

Differences between LDFSS and AUSM+ relate to the chosen functional forms for $U_k^{\pm}$ and $p_{k,1/2}$. Both, however, are grounded in the concept of a "numerical speed of sound" [19] that facilitates the shift from a discretization suitable for strongly compressible flows to one suitable for incompressible flows. Two numerical sound speeds, each associated with a particular phase and developed from the acoustic eigenvalues, are defined as follows:

$$\tilde{a}_{g,1/2} = \left(\sqrt{u_g^2 + 4\frac{\rho_b}{\rho_g}\beta_g^2} \right)_{1/2}, \tag{18}$$

$$\tilde{a}_{s,1/2} = \left(\frac{\sqrt{u_s^2(1 - M_{ref}^2)^2 + 4a_s^2 M_{ref}^2}}{1 + M_{ref}^2} \right)_{1/2}. \tag{19}$$

Quantities appearing in (18) and (19) are defined in Sections 3 and 4 and are arithmetically averaged to the cell interface. Other quantities needed in the LDFSS and AUSM+ formulations are phasic Mach numbers at left (L) and right (R) states

$$M_{k,\mathrm{L/R}} = \frac{u_{k,\mathrm{L/R}}}{\tilde{a}_{k,1/2}}, \tag{20}$$

and polynomials in Mach number [1]:

$$\mathscr{M}^{\pm}_{(1),k} = \frac{1}{2}(M_k \pm |M_k|), \tag{21}$$

$$\mathscr{M}^{\pm}_{(2),k} = \begin{cases} \pm\frac{1}{4}(M_k \pm 1)^2, & |M_k| < 1, \\ \mathscr{M}^{\pm}_{(1),k} & \text{otherwise}, \end{cases} \tag{22}$$

$$\mathscr{M}^{\pm}_{(4),k} = \begin{cases} \pm\frac{1}{4}(M_k \pm 1)^2 \pm \frac{1}{8}(M_k^2 - 1)^2, & |M_k| < 1, \\ \mathscr{M}^{\pm}_{(1),k} & \text{otherwise}. \end{cases} \tag{23}$$

The numerals in the subscripts of $\mathscr{M}$ indicate the degree of the polynomials.

From this, $U_k^{\pm}$ is defined for LDFSS as

$$U_k^{+} = \tilde{a}_{k,1/2}\left(\mathscr{M}^{+}_{(2),k,\mathrm{L}} - \mathscr{M}^{+}_{1/2}\right), \tag{24}$$

$$U_k^{-} = \tilde{a}_{k,1/2}\left(\mathscr{M}^{-}_{(2),k,\mathrm{R}} + \mathscr{M}^{-}_{1/2}\right), \tag{25}$$

where

$$\mathscr{M}^{+}_{1/2} = \mathscr{M}_{1/2}\left(1 - \frac{\Delta p_k + |\Delta p_k|}{2\rho_k \alpha_{k,\mathrm{L}} V^2_{\mathrm{ref},1/2}}\right), \tag{26}$$

$$\mathscr{M}^{-}_{1/2} = \mathscr{M}_{1/2}\left(1 + \frac{\Delta p_k - |\Delta p_k|}{2\rho_k \alpha_{k,\mathrm{R}} V^2_{\mathrm{ref},1/2}}\right) \tag{27}$$

and

$$\Delta p_k = p_{k,\mathrm{L}} - p_{k,\mathrm{R}}. \tag{28}$$

The notation $\mathscr{M}^{+}_{(2),k,\mathrm{L}}$ (for example) indicates the evaluation of the polynomial (22) using the phasic Mach number M_k at the left state. The function $\mathscr{M}_{1/2}$ is given as

$$\mathscr{M}_{1/2} = \frac{1}{4}\left[\sqrt{\frac{1}{2}(M^2_{k,\mathrm{L}} + M^2_{k,\mathrm{R}})} - 1\right]^2 \tag{29}$$

if both $|M_{k,\mathrm{L}}| < 1$ and $|M_{k,\mathrm{R}}| < 1$ and is zero otherwise. The function V^2_{ref} is equal to $\beta^2_{\mathrm{g}}(\rho_{\mathrm{b}}/\rho_{\mathrm{g}})$ for the gas-phase and $M^2_{\mathrm{ref}} a^2_{\mathrm{s}}$ for the solids-phase. As discussed in [14,15], the part of $U_k^{\pm}$ that is proportional to the pressure difference Δp_k (the "pressure diffusion" term) provides the necessary pressure–velocity coupling at very low speeds and facilitates monotone resolution of non-grid aligned discontinuities at higher speeds. The particular form is a modification of that presented in [2], following scaling arguments introduced in [15].

For AUSM+, $U_k^{\pm}$ is defined as

$$U_k^{+} = \tilde{a}_{k,1/2}\left(\max(0, \mathscr{M}^{+}_{(4),k,\mathrm{L}} + \mathscr{M}^{-}_{(4),k,\mathrm{R}}) + \frac{1 - M^2_{\mathrm{ref}}}{4}\mathscr{M}_{1/2}\frac{\Delta p_k}{\rho_k \alpha_{k,\mathrm{L}} V^2_{\mathrm{ref},1/2}}\right), \tag{30}$$

$$U_k^- = \tilde{a}_{k,1/2}\left(\min(0, \mathscr{M}^+_{(4),k,\mathrm{L}} + \mathscr{M}^-_{(4),k,\mathrm{R}}) + \frac{1-M_{\mathrm{ref}}^2}{4}\mathscr{M}_{1/2}\frac{\Delta p_k}{\rho_k \alpha_{k,\mathrm{R}} V^2_{\mathrm{ref},1/2}}\right), \tag{31}$$

where

$$\mathscr{M}_{1/2} = \mathscr{M}^+_{(4),k,\mathrm{L}} - \mathscr{M}^+_{(1),k,\mathrm{L}} - \mathscr{M}^-_{(4),k,\mathrm{R}} + \mathscr{M}^-_{(1),k,\mathrm{R}} \tag{32}$$

and all other quantities are as defined above for LDFSS. The multiplication of the pressure diffusion term by $1 - M_{\mathrm{ref}}^2$ serves to switch this term off whenever the local Mach number exceeds unity. For the incompressible gas-phase, the physical sound speed is assumed to approach infinity and M_{ref} is set to zero.

The proper choice of pressure splitting is a subject of current debate. Earlier works [14,15] have shown that the original Van Leer/Liou-type polynomial splittings lead to unphysical sources of numerical diffusion for low-Mach flows and can lead to scaling problems for real fluid flows. Modifications designed to prevent such adverse behavior have been proposed in [14,15] but all leave something to be desired. In this work, a more complete form for a general pressure splitting is presented and tested.

As a starting point, a general Van Leer/Liou-type polynomial splitting is defined for phase k as

$$p_{k,1/2} = \mathscr{P}^+_{(m),k,\mathrm{L}} p_{k,\mathrm{L}} + \mathscr{P}^-_{(m),k,\mathrm{R}} p_{k,\mathrm{R}}, \tag{33}$$

where $m = 1, 3,$ or 5 corresponds to polynomials of different degrees, defined as follows:

$$\mathscr{P}^{\pm}_{(1),k} = \begin{cases} \frac{1}{2}(1 \pm M_k), & |M_k| < 1 \\ \frac{1}{M_k}\mathscr{M}^{\pm}_{(1),k} & \text{otherwise,} \end{cases} \tag{34}$$

$$\mathscr{P}^{\pm}_{(3),k} = \begin{cases} \mathscr{M}^{\pm}_{(2),k}(\pm 2 - M_k), & |M_k| < 1 \\ \frac{1}{M_k}\mathscr{M}^{\pm}_{(1),k} & \text{otherwise,} \end{cases} \tag{35}$$

$$\mathscr{P}^{\pm}_{(5),k} = \begin{cases} \mathscr{M}^{\pm}_{(2),k}[(\pm 2 - M_k) \\ \quad \mp 3 M_k \mathscr{M}^{\mp}_{(2),k}], & |M_k| < 1 \\ \frac{1}{M_k}\mathscr{M}^{\pm}_{(1),k} & \text{otherwise.} \end{cases} \tag{36}$$

Eq. (33) can be rewritten without approximation as

$$p_{k,1/2} = \frac{1}{2}\left(\mathscr{P}^+_{(m),k,\mathrm{L}} - \mathscr{P}^-_{(m),k,\mathrm{R}}\right)(p_{k,\mathrm{L}} - p_{k,\mathrm{R}}) + \frac{1}{2}(p_{k,\mathrm{L}} + p_{k,\mathrm{R}})(\mathscr{P}^+_{(m),k,\mathrm{L}} + \mathscr{P}^-_{(m),k,\mathrm{R}}) \tag{37}$$

which can be further separated into cell-average plus diffusive components

$$p_{k,1/2} = \frac{1}{2}(p_{k,\mathrm{L}} + p_{k,\mathrm{R}}) + \frac{1}{2}\left(\mathscr{P}^+_{(m),k,\mathrm{L}} - \mathscr{P}^-_{(m),k,\mathrm{R}}\right)(p_{k,\mathrm{L}} - p_{k,\mathrm{R}}) + \frac{1}{2}(p_{k,\mathrm{L}} + p_{k,\mathrm{R}})\left(\mathscr{P}^+_{(m),k,\mathrm{L}} + \mathscr{P}^-_{(m),k,\mathrm{R}} - 1\right). \tag{38}$$

The third term on the right-hand side of (38) is the major problem, in that when the polynomials are evaluated using the phasic Mach numbers, the term may be excessively large for low-Mach flows. A better scaling, one also valid for real fluids, is found by replacing $(1/2)(p_{k,\mathrm{L}} + p_{k,\mathrm{R}})$ in this term by $\rho_k \tilde{a}^2_{k,1/2}$. The final form of the new pressure splitting is thus

$$p_{k,1/2} = \frac{1}{2}(p_{k,\mathrm{L}} + p_{k,\mathrm{R}}) + \frac{1}{2}\left(\mathscr{P}^+_{(m),k,\mathrm{L}} - \mathscr{P}^-_{(m),k,\mathrm{R}}\right)(p_{k,\mathrm{L}} - p_{k,\mathrm{R}}) + \rho_k \tilde{a}^2_{k,1/2}\left(\mathscr{P}^+_{(m),k,\mathrm{L}} + \mathscr{P}^-_{(m),k,\mathrm{R}} - 1\right). \tag{39}$$

This modification ensures that the second diffusive term will scale as the velocity magnitude as the Mach number becomes small. The new splitting represents an improvement over the linearized splittings presented in [15] in that the proper response at sonic transitions is ensured. One also can replace the cell-average pressure by $\rho_k V^2_{\mathrm{ref},1/2}$. At low Mach numbers, this will be less dissipative than the choice $\rho_k \tilde{a}^2_{k,1/2}$. The results presented in this paper use (39) exclusively, but there are indications that the choice $\rho_k V^2_{\mathrm{ref},1/2}$ may be better overall.

The current implementation for LDFSS uses the first-degree polynomials $\mathscr{P}^{\pm}_{(1),k}$ exclusively. The AUSM+ implementation tests all three polynomial forms.

5. Time integration

The schemes outlined in the previous section have been implemented into a code for solving time-dependent gas–solid flows. A dual time-stepping method is used to solve the following semi-discrete representation of (7)

$$\left(\frac{P}{\Delta\tau}\frac{\partial V}{\partial W}+\frac{1}{\Delta t}\frac{\partial U}{\partial W}+\frac{\partial \mathrm{R}}{\partial W}\right)\delta W^{n+1,m+1}=-\left(\frac{1}{\Delta t}(U^{n+1,m}-U^{n})+R^{n+1,m}\right), \tag{40}$$

$$W^{n+1,m}=W^{n,m}+\delta W^{n+1,m+1}. \tag{41}$$

In this, R is the steady-state residual, $\partial \mathrm{R}/\partial W$ is the associated Jacobian matrix, m is a subiteration index, n is the physical time index, $\Delta\tau$ is a local time step, Δt is the physical time step, and $W=[p_{\mathrm{g}},\alpha_{\mathrm{g}}u_{\mathrm{g}},\alpha_{\mathrm{g}}v_{\mathrm{g}},\alpha_{\mathrm{s}},\alpha_{\mathrm{s}}u_{\mathrm{s}},\alpha_{\mathrm{s}}v_{\mathrm{s}}]$. This choice of solution vector was found to be more stable than V given above.

Jacobian matrix entries corresponding to the convective terms in R are approximated as follows:

$$\frac{\partial F_{i+1/2}}{W_{i+1/2}}\delta W_{i+1/2}=\frac{1}{2}\left[\frac{\partial F}{\partial W}|_{i}+\Lambda_{i+1/2}\left(P\frac{\partial V}{\partial W}\right)_{i}\right]\delta W_i+\frac{1}{2}\left[\frac{\partial F}{\partial W}|_{i+1}-\Lambda_{i+1/2}\left(P\frac{\partial V}{\partial W}\right)_{i+1}\right]\delta W_{i+1} \tag{42}$$

with

$$\Lambda=\mathrm{diag}[\max|\lambda_{\mathrm{g}}|,\max|\lambda_{\mathrm{g}}|,\max|\lambda_{\mathrm{g}}|,\max|\lambda_{\mathrm{s}}|,\max|\lambda_{\mathrm{s}}|,\max|\lambda_{\mathrm{s}}|]. \tag{43}$$

This can be seen as a linearization of a modified Lax–Friedrichs flux for the preconditioned system, constructed so that the gas- and solids-phase components are each scaled by the corresponding maximum (in magnitude) eigenvalue. While not ideal, this approach provides a robust "driver" for the dual-time stepping algorithm. The linear system is approximately factored using an incomplete LU decomposition strategy at each physical time step. The factorization is stored over the duration of the subiterations to reduce CPU requirements. Typically, 25 to 35 subiterations are required to reduce the residual norm for the solids continuity equation one to two orders of magnitude.

6. Results

In this section, the methods outlined earlier are tested for several problems in fluidization. The first two problems, compaction of a solids bed and bubble formation within a two-dimensional fluidized bed, are chosen to test basic attributes of the numerical schemes. The remaining problems, bubble formation within a three-dimensional fluidized bed and gas–solid flow within the riser section of a circulating fluidized bed, are designed to evaluate the performance of the methods for more complicated situations.

6.1. Two-dimensional simulations

For the two-dimensional simulations, a rectangular 0.39×0.58 m^2 domain containing 65×65 mesh points is used for most calculations. Results from one calculation performed on a 129×129 grid are also presented. Nominal initial conditions are as follows:

$$
\begin{aligned}
0 \leqslant z \leqslant h_{\text{bed}}, \quad & \alpha_g = 0.44, \\
0 \leqslant x \leqslant 0.39, \quad & \alpha_s = 0.56, \\
& u_g = 0, \\
& \alpha_g v_g = 0.28 \text{ m/s}, \\
& u_s = 0, \\
& v_s = 0, \\
& p_g = p_\infty + \rho_s \alpha_s g (h_{\text{bed}} - z),
\end{aligned}
$$

$$
\begin{aligned}
h_{\text{bed}} < z < 0.58, \quad & \alpha_g = 0.999, \\
0 \leqslant x \leqslant 0.39, \quad & \alpha_s = 0.001, \\
& u_g = 0, \\
& \alpha_g v_g = 0.28 \text{ m/s}, \\
& u_s = 0, \\
& v_s = 0, \\
& p_g = p_\infty.
\end{aligned}
$$

Other necessary parameters are chosen as follows: d_p (particle diameter) $= 500$ μm, $\rho_s = 2660$ kg/m^3, $\rho_g = 1.235$ kg/m^3, $\mu = 20 \times 10^{-6}$ kg/(m s), $p_\infty = 101{,}000$ Pa. For these conditions, a minimum fluidization velocity of $u_{\text{mf}} = 0.64$ m/s is obtained [3], as is a minimum superficial fluidization velocity of $\alpha_g u_{\text{mf}} = 0.28$ m/s. Nominal boundary conditions are as follows:

$$
\begin{aligned}
0 < z < 0.58, \quad & \alpha_s \text{ extrapolated from interior}, \\
x = 0,\ x = 0.39, \quad & p_g \text{ extrapolated from interior}, \\
& u_g = 0, \\
& v_g \text{ extrapolated from interior}, \\
& u_s = 0, \\
& v_s \text{ extrapolated from interior},
\end{aligned}
$$

$$
\begin{aligned}
0 < x < 0.39, \quad & \alpha_s \text{ extrapolated from interior}, \\
z = 0, \quad & p_g \text{ extrapolated from interior}, \\
& u_g = 0, \\
& \alpha_g v_g = 0.28 \text{ m/s}, \\
& u_s \text{ extrapolated from interior}, \\
& v_s = 0,
\end{aligned}
$$

$$
\begin{aligned}
0 < x < 0.39, \quad & \alpha_s \text{ extrapolated from interior,} \\
z = 0.58, \quad & p_g = p_\infty \\
& u_g \text{ extrapolated from interior,} \\
& v_g \text{ extrapolated from interior,} \\
& u_s \text{ extrapolated from interior,} \\
& v_s = 0.
\end{aligned}
$$

These boundary conditions are applied at a cell interface using an array of ghost cells placed outside the physical domain. The exception is the gas pressure at the inflow ($z = 0$) boundary. Here, it is necessary to linearly extrapolate the gas pressure to the ghost cell to preserve the proper pressure–height relation.

The schemes are extended to second-order accuracy using standard slope-limiting procedures applied to the primitive variable vector V. Van Leer and Superbee limiters are used in the two-dimensional results that follow. The two-dimensional simulations are advanced in time using a fixed time step of 1×10^{-4} s, with 25 subiterations performed per time step. Larger numbers of subiterations changed the results only minimally.

Attention is focused primarily on the LDFSS implementation, with baseline parameters of $U_{\mathrm{ref,g}} = U_{\mathrm{ref,s}} = 5$ m/s, $C_s = 0.02$, $\tilde{\rho} = \bar{\rho} = \rho_b$. The baseline implementation also uses the $\mathscr{P}^{\pm}_{(1),k}$ polynomials and the Van Leer limiter. Selected calculations employ the AUSM+ extension.

6.1.1. Two-dimensional solids compaction

Fig. 1 displays results from a simulation of solids compaction in the bed (65×65 mesh) using the baseline LDFSS implementation with differing values of C_s. For this simulation, h_{bed} is taken as 0.41 m and the inflow superficial velocity is set to zero. The initial solids distribution thus moves downward under the influence of gravity until a balance between gas pressure, solids pressure, and gravitational force is achieved. The voidage pattern shown at the end of the simulation (15,000 iterations) is nominally steady, though some low-frequency oscillations still persist. The figure indicates that near maximum compaction is achieved at the bottom of the bed for low values of C_s. Decreases in C_s result in the sharpening of the final voidage profile.

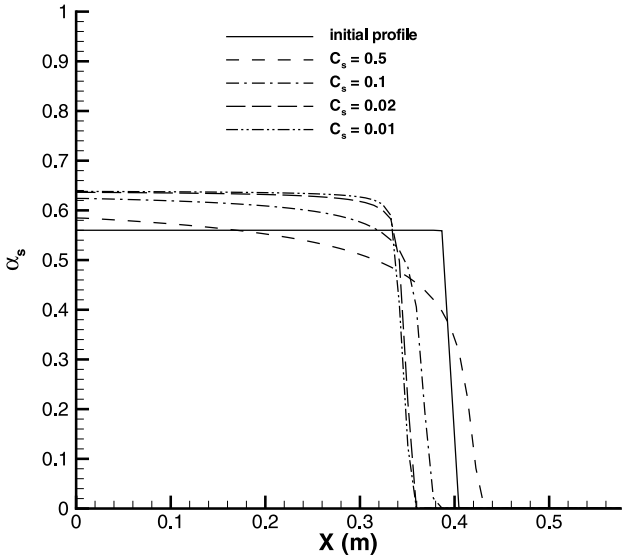

Fig. 1. Final voidage pattern for simulation of bed compaction.

6.1.2. Jet-induced bubble formation in a fluidized bed (2-D)

The next section of this paper discusses the performance of the developed techniques for the problem of jet-induced bubble formation in a minimally fluidized bed with h_{bed} equal to 0.29 m. This case has been studied by several authors under different conditions [6,20]. In the present work, a two-dimensional jet of width 0.015 m and superficial velocity 5.2 m/s is centrally located at the bottom of the bed and is introduced into the minimally fluidized bed at time $t = 0$. The jet induces the formation of several bubbles, which rise, deform, and collapse after reaching the surface. The results that follow present snapshots of the solids voidage at times $t = 0.3$, $t = 0.54$, and $t = 0.85$ s.

Fig. 2 compares baseline LDFSS results obtained on the 65×65 mesh with those obtained on the 129×129 mesh. The time step is halved for the calculation on the finer mesh to maintain the same CFL number. The top graph shows only the contour corresponding to a median "bubble edge" of $\alpha_s = 0.3$. The effects of mesh refinement are to sharpen the distinction between densely packed regions and more dilute regions, thus revealing more fine-scale structure, but otherwise, the time evolution is similar to the coarse-mesh results. The reader may compare the results that follow to the presumably more accurate calculations on the refined mesh to obtain an indication of the effects of the different parameter variations.

The calculations that follow utilize the 65×65 mesh exclusively. The effect of modifying $U_{ref,g}$ and $U_{ref,s}$ on the baseline LDFSS implementation on the 65×65 mesh is shown in Fig. 3. The reference velocities are set equal to one another and are varied from the baseline value of 5.0 m/s as shown. The reference solution is initially symmetric, but develops an asymmetry around $t = 0.54$ s which becomes more pronounced during the bubble collapse/solids spouting stage at $t = 0.85$ s. As the reference velocity is decreased, the computed bubbles become more rounded and are generally larger, and the solution retains its symmetry for longer periods of time. It is seen that the time evolution of the fluidized bed is altered for the lowest reference velocity. This may imply that the number of subiterations used (25) is insufficient to preserve proper time-accuracy for this choice of reference velocity.

Fig. 4 illustrates the effect of the choice of C_s on the baseline LDFSS solutions. This constant scales the solids sound speed and higher values imply that the solids-phase will respond in a more elliptic manner. In this figure and the next two, only the contour corresponding to a median "bubble edge" of $\alpha_s = 0.3$ is shown for reasons of clarity and brevity. As shown, the choice of $C_s = 0.1$ results in minimal bubble

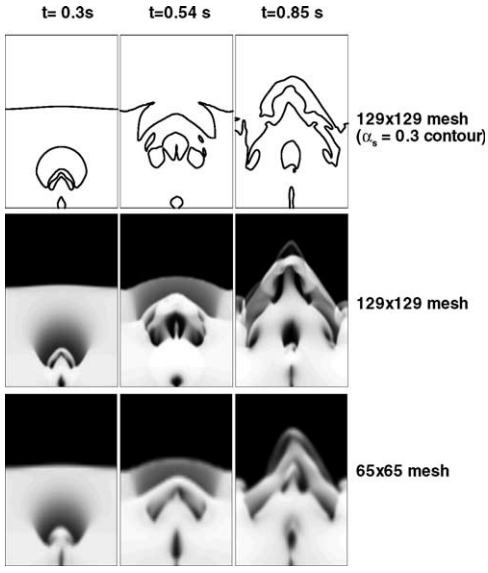

Fig. 2. Effect of mesh refinement on fluidized-bed response.

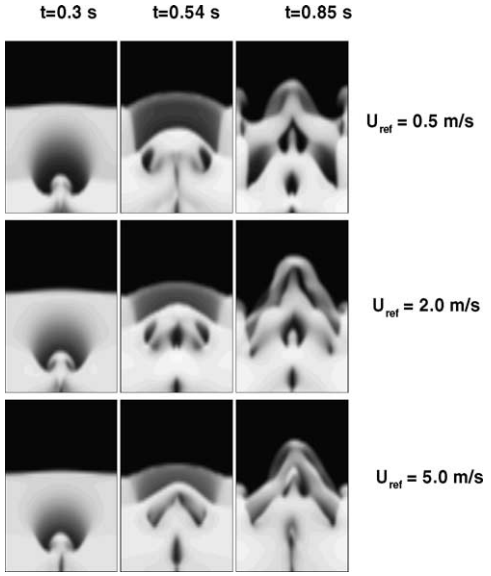

Fig. 3. Effect of reference velocity on fluidized-bed response.

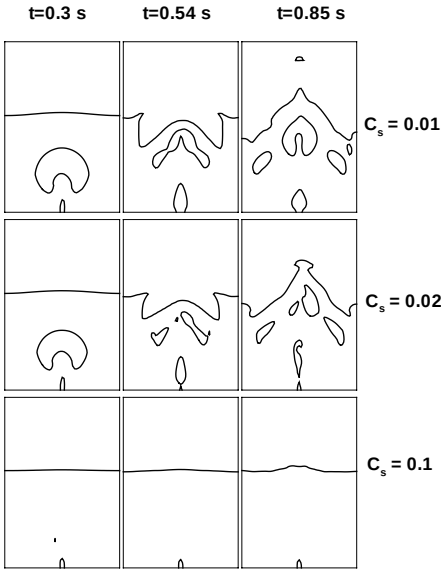

Fig. 4. Effect of C_s on fluidized-bed response (contour level corresponding to $\alpha_s = 0.3$).

growth. The lowering of C_s from the baseline value of 0.02 to 0.01 results in slightly larger bubbles and a more symmetric breakdown pattern.

The effect of the spatial accuracy of the LDFSS solution is shown in Fig. 5. The first-order solution maintains symmetry, but the generated bubbles are overly pointed at the centerline. As discussed in [6,21], this response is typical of first-order upwind methods applied to this problem and can be traced to excessive numerical diffusion in the solids momentum equation. Still, the first-order results presented here are no-

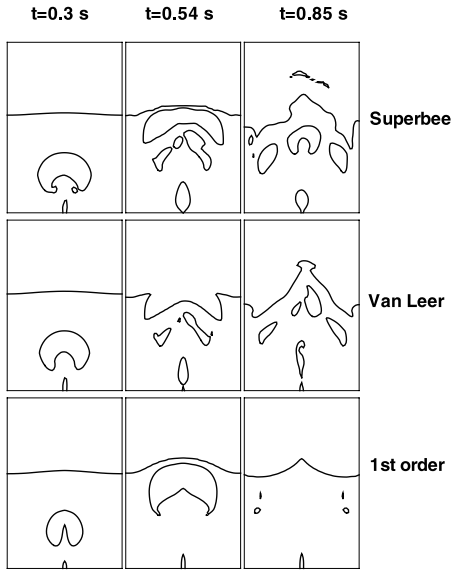

Fig. 5. Effect of spatial accuracy on fluidized-bed response (contour level corresponding to $\alpha_s = 0.3$).

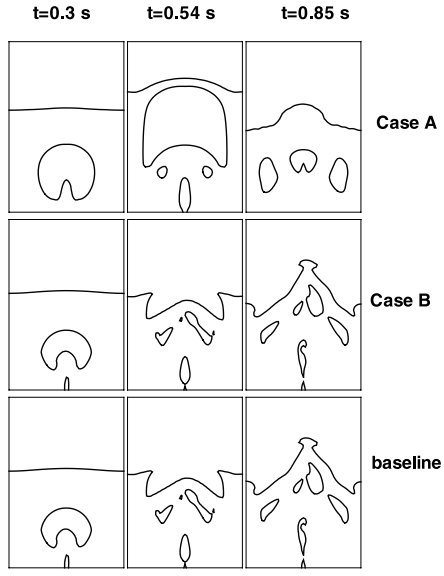

Fig. 6. Effect of reference density choice on fluidized-bed response (case A: $\rho_{RG} = \rho_g$, $\rho_{RS} = \rho_s$; case B: $\rho_{RG} = \rho_b$, $\rho_{RS} = \rho_s$; contour level corresponding to $\alpha_s = 0.3$).

ticeably better than the first-order solutions of [6]. The extension to second-order accuracy results in more rounded bubbles and a rapid breakdown to a non-symmetric, rather chaotic bubbling bed. The use of the Superbee limiter seems to accelerate the breakdown of the symmetric structure and results in generally more rounded bubbles.

Fig. 6 illustrates the effect of the choice of the reference densities $\tilde{\rho}$ and $\bar{\rho}$ on the fluidized-bed response. As discussed earlier, the choices of $\tilde{\rho} = \rho_g$ and $\bar{\rho} = \rho_s$ (Case A) render the eigenvalues independent of the

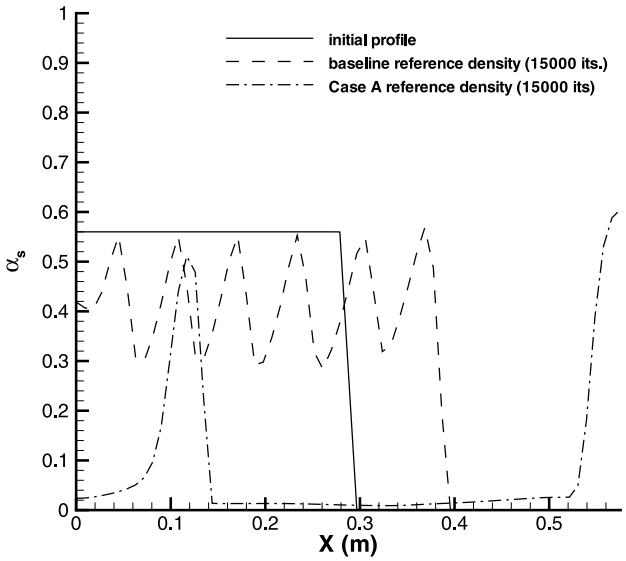

Fig. 7. Effect of reference density choice on 1-D fluidized-bed response (Case A: $\rho_{RG} = \rho_g$, $\rho_{RS} = \rho_s$).

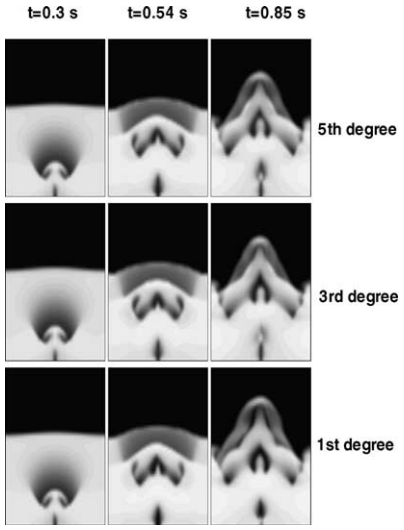

Fig. 8. Effect of pressure splitting on fluidized-bed response (AUSM+).

density. This prediction is different from the others in that the bed expands more with gas injection. The predicted bubble shapes are more rounded and the solution maintains its symmetry reasonably well. The choices of $\tilde{\rho} = \rho_b$ and $\bar{\rho} = \rho_g$ (Case B) result in predictions very similar to the baseline case. While the results for Case A appear promising at first glance, these choices do not respond as well in other tests. Fig. 7 displays results from a simulation in which the inflow superficial velocity is increased to two times the minimum fluidization velocity in the absence of the centerline jet. The expected result is a transient expansion of the fluidized bed to a new position. As predicted by the baseline formulation, this expansion is accompanied by transient bubble formation and collapse, and the position of the gas–solid interface

eventually oscillates about $z = 0.4$ m. Nevertheless, solids mass conservation is excellent (less than 0.2% mass loss/gain). In contrast, the choices of Case A result in an unphysical inversion of the bed, with a solids mass loss of 28%. The reasons for the failure of the more natural choices of $\tilde{\rho} = \rho_g$ and $\bar{\rho} = \rho_s$ to provide a proper response are not completely clear, but it is noteworthy that the gas-phase pressure diffusion terms in (26) and (27) are nearly fifty times larger for the Case A choices than for the baseline values.

Some results from the AUSM+ extension are shown in Fig. 8 for the same parameters as used in the baseline LDFSS scheme. Comparing Fig. 8 with Fig. 3, it can be seen that the predictions of AUSM+ are generally similar to those of LDFSS, though AUSM+ seems to capture some fine-scale features more sharply. One reason for this may be the inclusion of an additional diffusion mechanism, scaled by the absolute value of the interface pressure difference, in LDFSS. As discussed in [2], this term acts to suppress the "carbuncle" phenomenon often noted in supersonic blunt-body flows, but its utility in very low-speed calculations is questionable. Fig. 8 also shows that the effects of higher-degree pressure splittings on the AUSM+ predictions are minimal, though some evidence of increased numerical diffusion with the use of the higher-degree splittings is present in the form of slightly reduced bubble sizes.

6.2. Three-dimensional simulations

The remaining test cases focus on three-dimensional applications of the baseline LDFSS gas–solid algorithm ($C_s = 0.02$, Van Leer limiter). The three-dimensional algorithm is developed as a straightforward extension of the two-dimensional schemes and is parallelized for use on the North Carolina Supercomputing Center's IBM-SP2 using a MPI message-passing/domain-decomposition strategy.

6.2.1. Jet-induced bubble formation in a fluidized bed (3-D)

Parameters for simulation of three-dimensional bubble formation in a fluidized bed are the same as those listed above except for the following: d_p (particle diameter) = 800 μm, $\rho_s = 2420$ kg/m^3. The geometry is a $0.39 \times 0.39 \times 0.58$ m^3 rectangular box containing $65 \times 65 \times 65$ grid points, uniformly spaced in each direction. Nominal initial and boundary conditions are the same as mentioned earlier, except for the addition of slip surfaces corresponding to the third direction. A 5.77 m/s jet of air, exiting through a 0.0127×0.0127 m^2 square opening in the middle of the bottom plate, initiates bubble formation. Fig. 9 presents snapshots of solids void fraction along constant X, Y, and Z planes at different times after jet injection. As before, the initial response is the formation of a gas bubble which subsequently grows, then collapses near the end of the bed (Figs. 9(a) and (b)). After each subsequent bubble event, solids are entrained into the region occupied by the bubble, pinching off the jet and leading to the formation of a periodic sequence of smaller bubbles that eventually pass through the bed surface (Figs. 9(c) and (d)). As in the two-dimensional case, a spouting behavior is observed at later times (Figs. 9(d)–(f)). The LDFSS scheme, combined with the Van Leer limiter, captures the different stages of three-dimensional bubble formation with good resolution of gas–solid interfaces.

6.2.2. Gas–solid flow in the riser section of a circulating fluidized bed

The last test case corresponds to an experiment of Van den Moortel et al. [22] involving gas–solid flow within the riser section of a circulating fluidized bed. Prior computational results for this case have been presented by Zhang and VanderHeyden [8] using a similar hydrodynamics model and an Arbitrary Lagrangian/Eulerian (ALE) numerical method. The geometry is adapted from Zhang and VanderHeyden [8] and consists of an $H = 2$ m vertical riser with a 0.2×0.2 m^2 cross-sectional area. The cross-sectional area is linearly shrunk to 0.1×0.1 m^2 above 1.8 m. The calculation is initialized with 3% solids voidage, uniformly distributed within the riser. Other parameters are chosen as follows: d_p (particle diameter) = 120 μm, $\rho_s = 2400$ kg/m^3, $\rho_g = 1.200$ kg/m^3, $\mu = 18 \times 10^{-6}$ kg/(m s), $p_\infty = 101000$ Pa. As the iteration progresses, the solids mass flow rate calculated at the outflow is imposed at a vertical inflow plane (0.2×0.05 m^2) at the

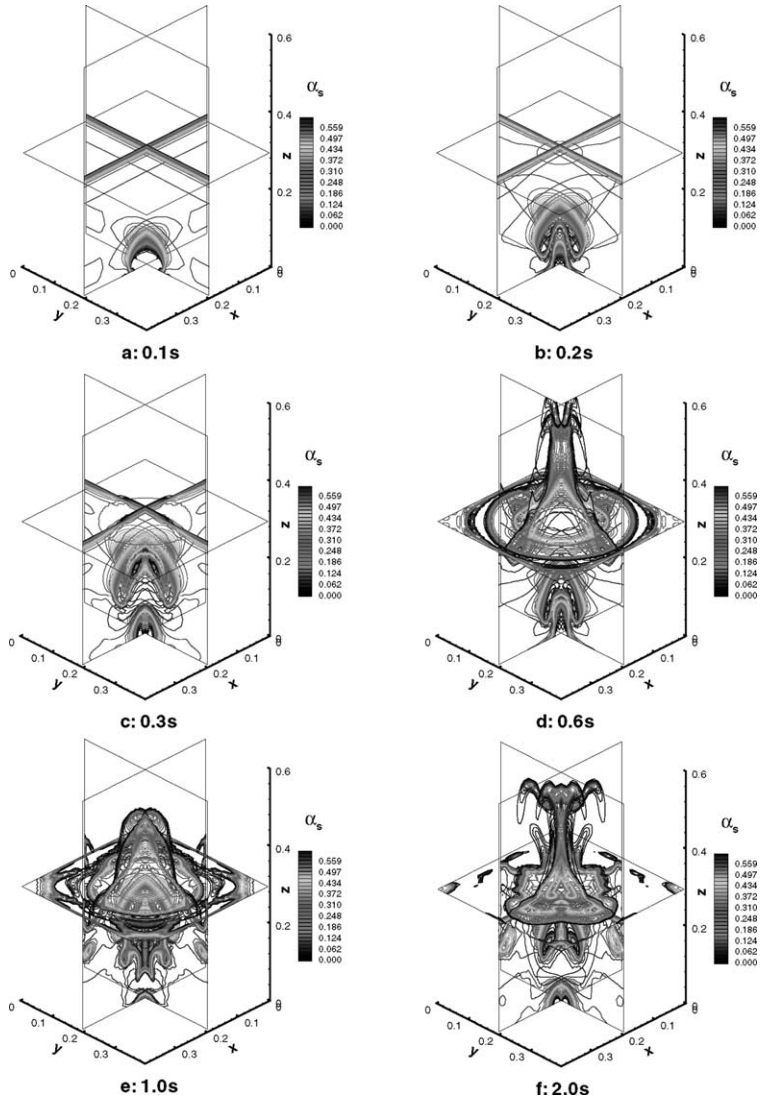

Fig. 9. Snapshots of solids voidage in simulation of three-dimensional fluidized bed.

bottom of the riser, thus simulating the recycling of the solids. After an initial period of time, the time-dependent solution reaches a statistically stationary state, characterized by a constant time-averaged solids mass flow rate. Fig. 10 shows snapshots of the logarithm of the solids void fraction during the start up period and after the system reaches a statistically steady state. The key features of the flowfield are elongated mesoscale structures containing higher solids concentrations. As expected, the solids voidage is highest near the bottom of the riser and near the walls, though a distinct core-annulus structure is not present. The LDFSS scheme (with $U_{\mathrm{ref,g}} = U_{\mathrm{ref,s}} = 15$ m/s) is clearly capable of capturing the fine-scale features of this complex flowfield. Fig. 11 compares the time-averaged solids mass flux obtained at different superficial gas velocities with experimental data. This quantity is obtained by dividing the time-averaged solids mass flow rate by the riser cross-sectional area. Good agreement with the experimental mass flux data is evidenced for the calculations performed with the Van Leer limiter. Results from calculations performed

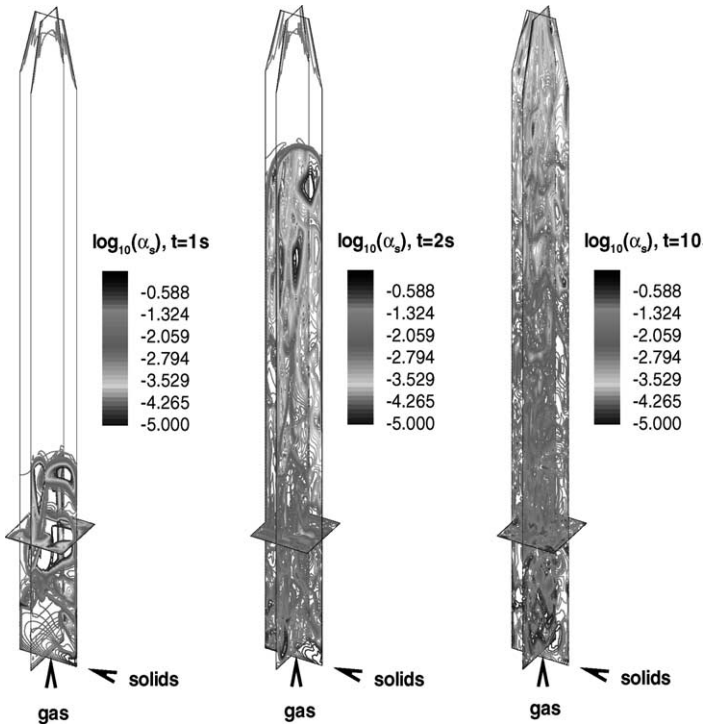

Fig. 10. Snapshots of solids voidage in simulation of three-dimensional circulating fluidized bed.

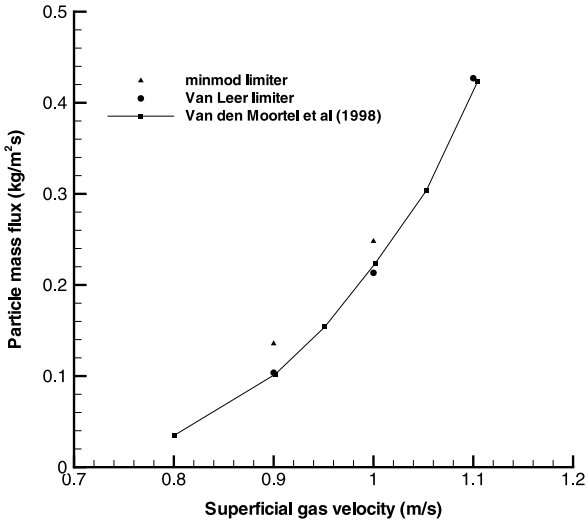

Fig. 11. Average mass flux at statistical steady state.

using the more dissipative minmod limiter display a consistent overprediction of the solids mass flux. Figs. 12 and 13 compare average solids vertical velocity at $z/H = 0.5$ and $z/H = 0.6$ with experimental data and predictions of Zhang and VanderHeyden [8]. The averages are computed as in [8], with

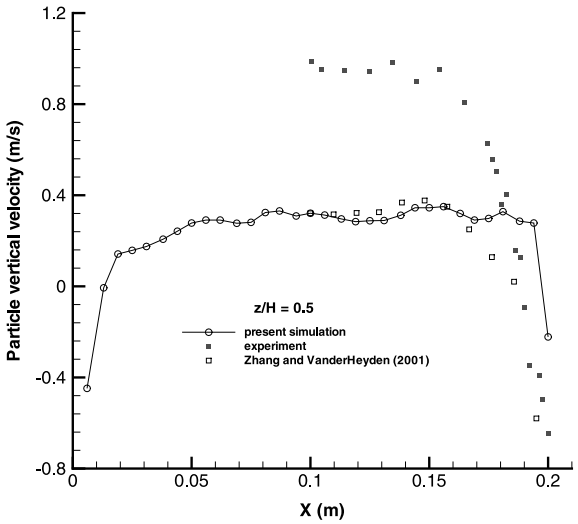

Fig. 12. Average solids vertical velocity at $z/H = 0.5$.

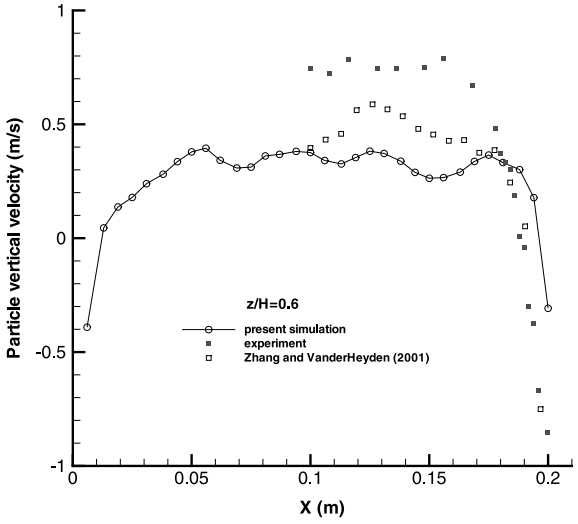

Fig. 13. Average solids vertical velocity at $z/H = 0.6$.

$$\langle \alpha_s \rangle_{i,j,k} = \sum_{n=1}^{N} (\alpha_s)^n_{i,j,k}, \tag{44}$$

$$\langle u_s \rangle_{i,j,k} = \frac{\sum_{n=1}^{N} (\alpha_s u_s)^n_{i,j,k}}{\langle \alpha_s \rangle_{i,j,k}}. \tag{45}$$

Computational predictions for vertical velocity are similar toward the middle of the riser but deviate near the boundary. This deviation may result in part from the fact that in the present calculation, solids are

injected through a small slot on the side wall as in the experiment, whereas in Zhang and VanderHeyden [8], solids are uniformly injected at the bottom of the riser. Agreement with averaged experimental vertical velocity data is only fair, but as noted in [22], standard deviations of the particle axial velocities are consistently of the order of the mean velocities, meaning that the concept of a velocity decomposition into mean and fluctuating components is questionable in itself. Further validation through simulations of other circulating fluidized bed flowfields may thus be required to quantify the accuracy of the present method.

7. Conclusions

A new approach for simulating dense gas–solid flows has been presented. The approach combines an artificial compressibility/preconditioning strategy for a particular two-phase flow model with extensions of the LDFSS and AUSM+ upwinding techniques. Simulations of bubble formation within a minimally fluidized bed have been conducted to illustrate different facets of the developed schemes. It is shown that the choice of reference velocity and the scaling of the solids sound speed both have marked effects on the ability of the schemes to capture the response of the bubbly bed properly. Values of the reference velocity of the order of the minimum fluidization velocity seem to promote more rounded bubble shapes, as do lower values of the solids sound speed scaling factor. As expected, higher-order simulations using the Van Leer and Superbee limiters provide a much more physically consistent response, and, somewhat surprisingly, the choice of reference density also impacts the quality of the simulations. Differences between LDFSS and AUSM+ predictions are found to be relatively minor. Three-dimensional simulations of bubble formation in a fluidized bed and hydrodynamics of a circulating fluidized bed have been presented to illustrate further the ability of the proposed techniques to capture complex gas–solid flowfields.

While somewhat specialized to a particular application in this work, many of the ideas presented herein should be directly extendible to other applications of low-diffusion upwinding techniques. More specifically, a new form of the pressure flux splitting has been developed that overcomes many of the scaling and consistency problems of earlier efforts, more self-consistent forms for adding pressure diffusion to the mass flux have been developed, and the concept of a ''numerical sound speed'' in enabling general low-Mach calculations has been extended to two-phase flows. These developments bring us one step closer to a unified, well-structured flux-splitting approach capable of handling gas-dynamic, real-fluid, and multiphase flows with equal ease.

Acknowledgements

This work has been sponsored by the US Environmental Protection Agency under cooperative agreement CR-82795701-0. IBM SP-2 computer time has been obtained through a grant from the North Carolina Supercomputing Center.

References

[1] M.S. Liou, A sequel to AUSM: AUSM+, J. Comp. Fluids 129 (1996) 23.
[2] J.R. Edwards, A low-diffusion flux-splitting scheme for Navier–Stokes calculations, Comput. Fluids 26 (1997) 635.
[3] D. Gidaspow, Multiphase Flow and Fluidization, Academic Press, Boston, 1994.
[4] J.L. Sinclair, R. Jackson, Gas-particle flow in a vertical pipe with particle–particle interactions, AIChE J. 35 (1989) 1473.
[5] J. Ding, D. Gidaspow, A bubbling fluidization model using kinetic theory of granular flow, AIChE J. 36 (1990) 523.
[6] C. Guenther, M. Syamlal, The effect of numerical diffusion on simulation of isolated bubbles in a gas–solid fluidized bed, Powder Tech. 116 (2001) 142.

[7] B.G.M. van Wachem, J.C. Schouten, R. Krishna, C.M. van den Bleek, Eulerian simulations of bubbling behavior in gas–solid fluidized beds, Comput. Chem. Eng. 22 (1998) 5299.
[8] D.Z. Zhang, W.B. VanderHeyden, High-resolution three-dimensional numerical simulation of a circulating fluidized bed, Powder Tech. 116 (2001) 133.
[9] L. Combe, J.-M. Herard, Finite volume algorithm to compute dense compressible gas–solid flows, AIAA J. 37 (1999) 337.
[10] S. Boivin, F. Cayre, J.-M. Herard, Un schema volumes finis pour la simulation d'ecoulements diphasiques gaz particules a deux phases incompressibles sur maillage triangulaire, Eur. J. Finite Elem. 10 (2001) 539, also AIAA Paper 2000–2665 (unpublished).
[11] E. Turkel, Preconditioned methods for solving the incompressible and low speed compressible equations, J. Comput. Phys. 72 (1987) 277.
[12] Y.H. Choi, C.L. Merkle, The application of preconditioning in viscous flows, J. Comput. Phys. 105 (1993) 207.
[13] J.M. Weiss, W.A. Smith, Preconditioning applied to variable and constant density flows, AIAA J. 33 (1995) 2050.
[14] J.R. Edwards, M.-S. Liou, Low-diffusion flux-splitting methods for flows at all speeds, AIAA J. 36 (1998) 1610.
[15] J.R. Edwards, R.K. Franklin, M.-S. Liou, Low-diffusion flux-splitting methods for real fluid flows with phase transitions, AIAA J. 38 (2000) 1624.
[16] Y.Y. Niu, Advection upwinding method to solve a compressible two fluid model, Int. J. Numer. Meth. Fluids 36 (2001) 351.
[17] H. Paillere, C. Corre, J. Garcia Cascales, On the extension of the AUSM+ scheme to compressible two-fluid models, Computers & Fluids, in press.
[18] J. De Wilde, J. Vierendeels, E. Dick, An extension of the preconditioned AUSM to two-phase flows for the 3D calculations of circulating fluidized beds, Third International Symposium on Computational Technologies for Fluid/Thermal/Chemical Systems with Applications, ASME-PVP, 2001.
[19] M.-S. Liou, J.R. Edwards, Numerical speed of sound and its application to schemes for all speeds, AIAA Paper 99-3268 (unpublished).
[20] D. Gidaspow, M. Syamlal, Y.C. Seo, Hydrodynamics of fluidization: supercomputer generated vs. experimental bubbles, J. Powder Bulk Solids Tech. 10 (1986) 19.
[21] I. Christie, G.H. Ganser, J.W. Wilder, Numerical solution of a two-dimensional fluidized bed model, Int. J. Numer. Meth. Fluids 28 (1998) 381.
[22] T. Van den Moortel, E. Azario, R. Santini, L. Tadrist, Experimental analysis of the gas-particle flow in a circulating fluidized bed using a phase Doppler particle analyzer, Chem. Eng. Sci. 53 (1998) 1883.